

Tracking coherent structures in massively-separated and turbulent flows

Matthew Rockwood,^{*} Yangzi Huang, and Melissa Green

Mechanical and Aerospace Engineering Department, Syracuse University, Syracuse, New York 13244, USA



(Received 30 June 2017; published 29 January 2018)

Coherent vortex structures are tracked in simulations of massively-separated and turbulent flows. Topological Lagrangian saddle points are found using intersections of the positive and negative finite-time Lyapunov exponent ridges, and these points are then followed in order to track individual coherent structure motion both in a complex interacting three-dimensional flow (turbulent channel) and during vortex formation (two-dimensional bluff body shedding). For a simulation of wall-bounded turbulence in a channel flow, tracking Lagrangian saddles shows that the average structure convection speed exhibits a similar trend as a previously published result based on velocity and pressure correlations, giving validity to the method. When this tracking method is applied in a study of a circular cylinder in cross-flow it shows that Lagrangian saddles rapidly accelerate away from the cylinder surface as the vortex sheds. This saddle behavior is compared with the time-resolved static pressure distribution on the circular cylinder, yielding locations on a cylinder surface where common sensors could detect this phenomenon, which is not available from force measurements or vortex circulation calculations. The current method of tracking coherent structures yields insight into the behavior of the coherent structures in both of the diverse flows presented, highlighting the breadth of its potential application.

DOI: [10.1103/PhysRevFluids.3.014702](https://doi.org/10.1103/PhysRevFluids.3.014702)

I. INTRODUCTION

Coherent vortex structures are a key component of unsteady flows that include propulsive wakes, flow separation, or instabilities in shear layers. They play an important role in fluid mixing and instability, kinetic energy production and dissipation, mass transport and diffusion, and force production. Coherent structures are often found in the wake of bluff bodies, aerodynamic surfaces at high angles of attack, or in turbulent flows. Generally these coherent structures produce negative effects, such as oscillating forces, when they interact with aerodynamic bodies, but they can also provide beneficial effects such as enhanced mixing and mass or momentum transport. The visualization and tracking of coherent structures helps to explain the basic physics of turbulent motions and can be used to improve turbulent flow modeling, prediction, and the design and implementation of control systems. Consequently, an understanding of the behavior of coherent structures can aid in the design of high-lift devices or artificial adaptation of biologically inspired flexible control surfaces, among other applications.

Although studies on vortex dynamics have been carried out for decades, a widely accepted, objective definition of a vortex and its boundaries remains an open question. Techniques used to define vortices are generally broken down into Eulerian and Lagrangian analyses. Eulerian vortex identification techniques use the instantaneous velocity field and its gradients to identify regions that contain vortices, while Lagrangian vortex identification techniques calculate particle trajectories using multiple velocity fields to determine which regions of the flow are dynamically distinct. A

^{*}mprockwo@syr.edu

combination of Eulerian and Lagrangian techniques has previously been found to be useful when studying the cylinder near-wake and flow separation [1–3].

Many Eulerian vortex criteria identify the coherent structures by a local swirling motion, which has the presence of closed or spiral streamlines or path lines in a suitable reference frame. Graftieaux *et al.* [4] defined a scalar function Γ_1 by using the topology of the velocity field to yield the center of the vortex core. The Q criterion, developed by Hunt *et al.* [5], identifies regions as vortices if the norm of the local rate of rotation tensor is dominant over the norm of the local rate of strain. While these techniques can quickly identify regions of the flow that contain coherent structures, they generally require a suitable frame of reference and a carefully selected threshold. Some examples of work studying vortex formation using Eulerian techniques include studies on cylinders [6,7] and rapidly pitching airfoils [8].

Alternatively, there exist several Lagrangian methods that are based on the quantities calculated along fluid particle trajectories, including calculation of the finite-time Lyapunov exponent (FTLE). Maximizing ridges of FTLE have been shown to represent transport boundaries in vortex-dominated flows [9,10]. Many Lagrangian quantities, including FTLE, rely on the calculation of the flow map: the vector quantity defined at each point in space specifying where a particle trajectory initialized at that point would be located after an integration time τ . In an attempt to rectify errors in the flow map caused by the low number of trajectories common to oceanic flows, Allshouse and Thiffeault [11] developed a method to detect coherent structures using a three-dimensional braid structure constructed from two-dimensional trajectories. This braid structure was then used to detect non-growing topological loops that enclosed invariant regions. Further investigation of these types of loops determined that in two-dimensional turbulent flows these coherent Lagrangian vortices can travel through the flow without being destroyed [12,13]. This type of analysis has been extended to three-dimensional unsteady flows in an investigation of hyperbolic and elliptic transport barriers [14].

In previous studies, FTLE analysis and its related Lagrangian coherent structure (LCS) analysis have been applied to study the unsteady wakes behind a pitching panel [15], a cylinder [16–19], oceanic eddies [20], aortic valve jets [21], flow separation [2,3,22], fluid transport of translating and flapping wings [23], non-axisymmetric vortex rings [24], dynamic stall [25], and hurricanes [26]. A review of different methods for finding LCSs has been recently published by Allshouse and Peacock [27]. The variational theory method proposed by Haller [28] found an exact relationship between the LCS and the invariants of the Cauchy-Green strain tensor that allowed for LCSs to be defined as the locally strongest attracting or repelling material surfaces, and Wang *et al.* [29] showed that LCSs implemented with a closed-loop control scheme can change the flow structure dramatically in the wake of a bluff body. In the case of piston generated vortex rings [30], it was observed that the separation of multiple LCSs was a precursor to the formation of a secondary discrete vortex in the flow. Previous studies analyzed the flow around both a flat plate undergoing a 45° pitch-up maneuver [31] and a wing undergoing dynamic stall [25] using both Eulerian and Lagrangian techniques to identify the primary leading-edge vortex (LEV) and its dynamics. The departure of Lagrangian saddles from near the leading edge corresponded to the shedding of the LEV as well as to a decrease in the lift generated by the plate. While current computational systems can efficiently process the velocity information needed to track trajectories for these Lagrangian calculations, improvements in experimental techniques have led to increasingly large amounts of data, requiring development of automated procedures for vortex tracking [32].

Lagrangian techniques have been shown to help identify and describe mass transport and vortex dynamics in a variety of unsteady flow fields, but they are more computationally intensive than Eulerian techniques and require future data when calculating forward-time quantities. In the present study, the method of coherent structure tracking using Lagrangian saddles is established in a three-dimensional turbulent channel flow simulation. The average convection speed of vortices is computed as a function of wall-normal distance and is compared to previously published work for validation. The case of vortex shedding from a circular cylinder is then considered using the same technique in order to relate the vortex dynamics as tracked by the Lagrangian saddles to surface pressure measurements. A quantity such as static pressure is measurable using common sensors and therefore

the demonstrated connection between the Lagrangian saddle motion and the time history of surface measurements indicates how one might track the behavior of vortices in real time.

II. METHODS

Several vortex identification techniques have been applied to the results from two unsteady-flow simulations to maximize the information gathered on the flow physics. Several Eulerian criteria have been used in similar analyses previously (Q [5], Δ [32], λ_2 [33], Γ_1 [4]), but do not yield distinctly dissimilar results, and for this work, the Q criterion is chosen for simplicity and for consistency with similar studies in the literature. The Q criterion is a scalar quantity based on the instantaneous velocity field gradient that identifies a positive-valued region as containing a vortex core, as described below. Circulation is an integrated scalar quantity that is a measure of the flux of vorticity through an area boundary, and it can be used as a measure of the strength of the vortex. The FTLE is a scalar field that highlights the boundaries of vortices. Each of these techniques provides useful information about the flow physics and is explained in more detail below.

A. Q criterion: Vortex area and core location

The Q criterion, an Eulerian scalar, identifies regions of the flow as vortices when there is local rotational motion. The velocity gradient tensor $\nabla \mathbf{u}$ is decomposed into the symmetric rate of strain tensor \mathbf{S} and antisymmetric rate of rotation tensor $\mathbf{\Omega}$ as

$$\nabla \mathbf{u} = \mathbf{S} + \mathbf{\Omega}, \quad (1)$$

where $\mathbf{S} = \frac{1}{2}[\nabla \mathbf{u} + (\nabla \mathbf{u})^*]$ and $\mathbf{\Omega} = \frac{1}{2}[\nabla \mathbf{u} - (\nabla \mathbf{u})^*]$. In this equation $(\)^*$ is used to denote the transpose operator. Using these relationships, the Q value is defined as

$$Q = \frac{1}{2}[\|\mathbf{\Omega}\|^2 - \|\mathbf{S}\|^2], \quad (2)$$

where $\|\mathbf{\Omega}\|$ represents the Euclidean norm of $\mathbf{\Omega}$ (sometimes known as the Frobenius norm). Vortices are found where the norm of the local rate of rotation tensor is dominant over the norm of the local rate of strain tensor [5]. These regions, where $Q > 0$, indicate where local rotation dominates over local strain and are defined as being within a vortex using this method.

In simple flows, especially simulations in two dimensions, contours of $Q = 0$ can often be plotted as vortex boundaries. In complex flows, notably three-dimensional or turbulent experimental flows, contours of a certain percentage of the global Q_{\max} are often used (for example, $0.1 Q_{\max}$) to help filter out noise in the system caused by uncertainty in the velocity measurements. The center of a vortex is tracked in Sec. IV of this paper by finding the location of the maximum value of Q within a vortex, and this method works well in the simple two-dimensional simulation of a cylinder at low Reynolds number. In more complex cases, especially with experimental data, this would be impractical since the maximum Q value might not necessarily be located in the central region of the vortex and can vary dramatically due to errors in the calculation of velocity gradients.

B. Circulation: Measure of vortex strength

Circulation can be used as a metric of vortex strength by measuring the vorticity flux into a prescribed area defined by the boundaries of the vortex. In the case of a circular cylinder, the vorticity flux is caused by the transport of vorticity generated in the shear layer along the cylinder surface into the forming vortex. Circulation is defined as

$$\Gamma = \iint_A \boldsymbol{\omega} \cdot d\mathbf{A}, \quad (3)$$

where $\boldsymbol{\omega}$ is the vorticity and $d\mathbf{A}$ is the normal vector to an infinitesimal portion of the area, A . When calculating circulation, especially when comparing values over time, special care must be taken to consider the circulation inside a consistently defined area. There is no clear definition of a

vortex boundary that is used to determine the correct area for all circulation calculations, and this is further complicated if a shear layer is feeding the vortex, as the boundary between the vortex and the shear layer is unclear and often defined in a subjective or application-specific manner. Generally a bounding box is drawn large enough to encompass the entire vortex while still eliminating as much of any nearby, but distinct, regions of vorticity as possible, such as a feeding shear layer [34].

C. Finite-time Lyapunov exponent: Vortex boundaries

The FTLE measures the maximum rate of separation around a certain location in space (\mathbf{x}_0) by first calculating the flow map of neighboring particles $\phi(\mathbf{x}_0, t_0, \tau)$ over an integration time τ , and constructing the Cauchy-Green strain tensor from the spatial gradient of the flow map. The maximum eigenvalue of the Cauchy-Green strain tensor is referred to as the coefficient of expansion, σ_τ :

$$\sigma_\tau(\mathbf{x}_0, t_0, \tau) = \lambda_{\max} \left(\left[\frac{\partial \phi(\mathbf{x}_0, t_0, \tau)}{\partial \mathbf{x}_0} \right]^* \left[\frac{\partial \phi(\mathbf{x}_0, t_0, \tau)}{\partial \mathbf{x}_0} \right] \right). \quad (4)$$

From there, the FTLE field is defined from the coefficient of expansion as

$$\Lambda(\mathbf{x}_0, t_0, \tau) = \frac{1}{2\tau} \ln \sigma_\tau(\mathbf{x}_0, t_0, \tau). \quad (5)$$

Maximizing ridges in this field indicate high levels of Lagrangian stretching among nearby particle trajectories and have been shown to represent transport boundaries in vortex-dominated flows [9,10]. It is important to note that changing the threshold value for FTLE ridge extraction does not change the location of the coherent structures identified, only the thickness of the ridge visualization.

While repelling ridges of the FTLE can be calculated using forward-time integration, attracting ridges at time t_0 can be found by calculating the FTLE using particle trajectories initialized at t_0 and integrated in negative time. This calculation also yields a scalar FTLE field, but because it measures Lagrangian separation in negative time, its ridges represent those regions in the flow where particle trajectories are being attracted, as opposed to being repelled. By including ridges from both FTLE calculations, the analysis produces both the repelling FTLE ridges at t_0 along which particle trajectories locally will separate from each other (positive time, pFTLE) and the attracting FTLE ridges at t_0 along which particle trajectories locally have contracted to each other (negative time, nFTLE). The pFTLE and nFTLE ridges at time t_0 intersect at the outer boundaries of vortices but do not overlap. Inclusion of both FTLE types provides a more complete boundary that delineates which particles are entrained into the vortex from those that continue to convect with the outer flow. Since the Q criterion only visualizes the vortex cores, the ability to visualize the boundaries objectively provides additional insight into the vortex dynamics, especially when studying the interactions among coherent structures. A representation of the vortex boundaries using FTLE ridges is obtained at later times in the flow evolution by reinitializing the flow map calculations (updating t_0), which is considered the “standard” method by Lipinski and Mohseni [35]. The FTLE has been demonstrated to be robust to velocity field errors that are small in magnitude or short in duration [10]. Having poor spatial or temporal resolution can have a negative effect on the exact FTLE ridge location, but the mean location of the FTLE ridge is not affected by noise levels below 10% of the vortex convection speed [36].

Vortex structures are tracked using points where the nFTLE ridges intersect with the pFTLE ridges. These intersections of the attracting and repelling ridges in the flow are Lagrangian saddles and have been shown to be dynamically important features that are a component of vortex boundaries [15]. In the current study, Lagrangian saddles are found by locating a neighboring set of points that have sufficiently high values of both pFTLE and nFTLE, and then finding the center of this region. Miron and Vétel [2] found that these Lagrangian saddles are not always found using Eulerian techniques, and their behavior in space and time has previously been shown to provide insight into the time of vortex shedding [31]. The behavior of material particles initially located in the vicinity of a Lagrangian saddle is shown in Fig. 1. Each quadrant of particles around the saddle point is colored one solid

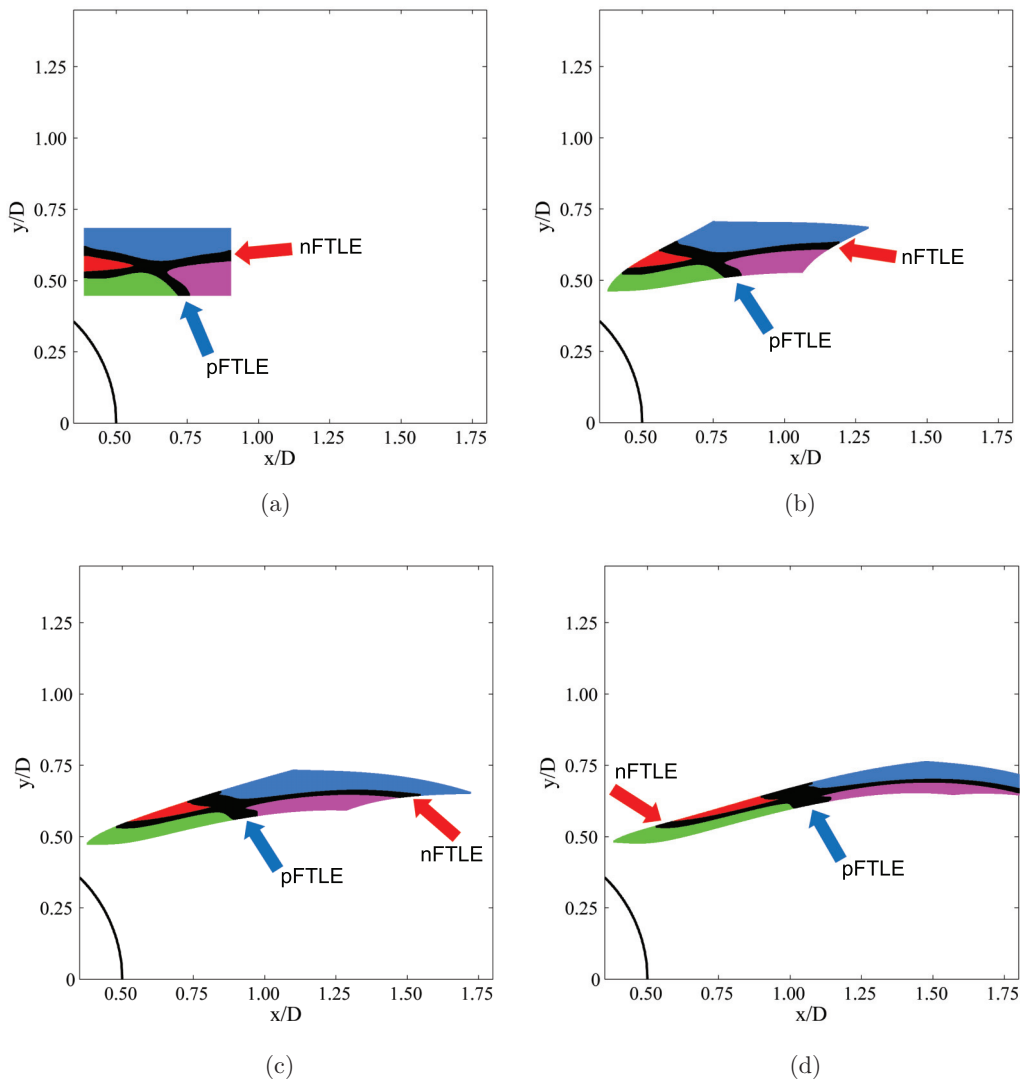


FIG. 1. Lagrangian particle evolution around a Lagrangian saddle: (a) $t/T = 0.75$, (b) $t/T = 0.82$, (c) $t/T = 0.89$, and (d) $t/T = 0.96$. Particles with values above $0.75\Lambda_{\max}$ are black; other particles are colored by their initial location. Repulsion from the pFTLE ridge is indicated by the thickening of the black ridge between red and blue, and between green and magenta. Attraction to the nFTLE ridge is indicated by the narrowing of the black ridge between red and green, and between blue and magenta.

color, and any particles found near an FTLE ridge ($\Lambda \geq 0.75\Lambda_{\max}$) are colored black. There is a clear motion of particles away from the pFTLE ridge [top left to bottom right in Fig. 1(a)] and along the nFTLE ridge [top right to bottom left in Fig. 1(a)], which agrees with the expected behavior of particles in the vicinity of a Lagrangian saddle. This is further observed in the thickening of the region initially containing particles near the pFTLE ridge as the nearby particles are repelled away, and a narrowing of the region initially containing particles near the nFTLE ridge as the particles are attracted closer. This trend holds over the entire integration time. In general, multiple Lagrangian saddles can be found along a vortex-bounding FTLE ridge, even in relatively simple flows such as the von Kármán vortex street behind a circular cylinder. Tracking any of the Lagrangian saddles can

indicate the motion of the vortex boundary, but in the examples shown here only the locations of the upstream saddle have been observed to be related to the vortex shedding time in massively-separated flows.

III. TRACKING MULTIPLE VORTEX STRUCTURES IN COMPLEX THREE-DIMENSIONAL FLOWS

Fully developed three-dimensional channel flow has been studied extensively to increase the understanding of the basic physics of wall-bounded turbulent flows. Structure identification and tracking in the channel flow is important for the quantitative and qualitative investigations of complex turbulence interactions near a wall, as well as for the design and testing of turbulence closure models, independent of whether the flow is treated as a stochastic flow field, a network of coherent structures, or a superposition of waves [37,38].

The convection velocity of coherent structures is of fundamental interest as vortex structures play a dominant role in transport phenomena in turbulent flows. As indicated in the literature [38], individual vortex structures are not expected to propagate at the speed of the mean flow. The velocity of structures varies among vortices, and for one given vortex, its convection velocity will change with time and location in a turbulent channel flow. Kim *et al.* [39] and Kim and Hussain [40] previously showed the variation of average structure convection velocity with wall-normal distance in turbulent channel flow using space-time correlations of velocity and pressure fluctuations. Their study found that structure convection velocity is slightly less than the local mean velocity for most of the channel, except in the near-wall region. The current study also calculates the streamwise structure convection velocity, here using cross correlations of Lagrangian saddle locations.

Here, the temporally and spatially averaged convection velocity is measured on two-dimensional planes parallel to the wall. This is accomplished by tracking Lagrangian saddles in each plane to determine their average streamwise velocities. The statistical average of the convection velocity has practical application, such as in aeroacoustic studies where structure velocity can indicate the time and velocity scales of the most dominant features that produce aerodynamic forces and sound [40].

The three-dimensional, fully turbulent channel simulation for this study was run at $Re_\tau = 180$, with $Re_\tau = u_\tau h / \nu$, where u_τ is the friction velocity, h is the channel half height, and ν is the kinematic viscosity. In these quantities, $u_\tau = (\tau_w / \rho)^{1/2}$, where τ_w is the shear stress at the wall and ρ is the density. The computational domain is $x/h \in [0, 2\pi]$ in the streamwise direction, $z/h \in [0, 2\pi]$ in the spanwise direction, and $y/h \in [-1, 1]$ in the wall-normal direction. It is bounded by walls at $y/h = -1$ and $y/h = 1$ and has periodic boundary conditions in the streamwise and spanwise directions. Distance from the wall can also be represented in terms of $y^+ = u_\tau y / \nu$.

This simulation was used by Green *et al.* [41] and was based on that of Kim *et al.* [39]. For the case shown here, a non-dimensional integration time of $\tau^+ = 27$ was used for the flow map computation with integration time steps of $\Delta t^+ = 0.09$. Both integration time and time steps were non-dimensionalized as $t^+ = tu_\tau^2 / \nu$. The integration time was chosen based on previous results, and it yields well-defined FTLE fields. As can be seen in Fig. 2, shorter integration times can result in less sharp FTLE ridges, but by $\tau^+ = 27$, the FTLE ridges are converged. Longer integration of the flow map to $\tau^+ = 36$ or $\tau^+ = 45$ does not change the ridge locations, only sharpens them. The values of FTLE along the ridges decrease, which can be expected because the denominator of Eq. (5) is increasing, but the particle trajectories that were initialized near the ridges may have left the vicinity of structures and may not be continuing to separate.

Results

In this study, the averaged structure convection velocity at each wall-normal location was found by tracking the Lagrangian saddles in wall-parallel planes of the channel flow. Fields of nFTLE in these data were originally presented by Green *et al.* [41], but the current study manages to detect and track Lagrangian saddles automatically from processed nFTLE and pFTLE data sets. Figure 3

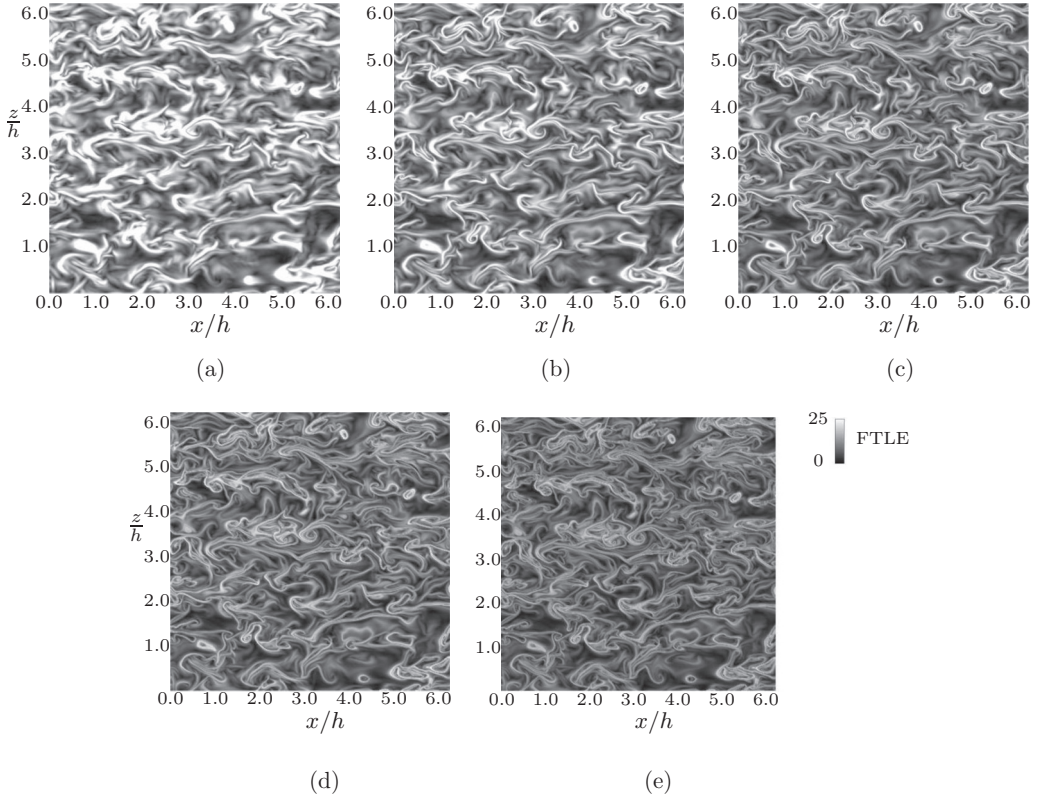


FIG. 2. Negative-time FTLE fields in a plane located at $y^+ = 49.6$ for five different integration times: (a) $\tau^+ = 9$, (b) $\tau^+ = 18$, (c) $\tau^+ = 27$, (d) $\tau^+ = 36$, and (e) $\tau^+ = 45$. All five panels use the same color axis as shown.

shows FTLE ridges in wall-parallel two-dimensional planes at $y^+ = 10.5$ and $y^+ = 49.6$ in the turbulent channel at one representative time. Positive- and negative-time FTLE ridges are shown as blue and red curves, respectively, and cyan dots locate the Lagrangian saddles at the intersections of the pFTLE and nFTLE ridges. While two-dimensional cuts of the FTLE surfaces are shown here as FTLE ridges, the full three-dimensional domain is used for the FTLE calculation.

The ridges of the FTLE field are co-dimension-1 structures, meaning that in two-dimensional flows, they are one-dimensional curves. In the case of the turbulent channel, which is three dimensional, the FTLE ridges will be two-dimensional curved surfaces in space. In Fig. 3, although the flow maps were only initialized in a series of single planes, they were advected in the full three-dimensional data domain. For this reason, the ridges in Fig. 3 can be considered the intersection of the two-dimensional surfaces of the FTLE ridges with these particular planes. The saddles, which are the intersections of the FTLE ridges, are co-dimension 2, meaning that they are points in two-dimensional flows, and one-dimensional line segments in three-dimensional flows. The saddle points of Fig. 3 are then intersections of the saddle curves with the shown two-dimensional planes. It is expected that the saddle line segments will have some movement in the wall-normal direction, and therefore the streamwise velocity could also be including line segment growth, bending, or rotation. The results obtained from the numerical hotwires used by Kim and Hussain [40], however, would be subject to the same errors.

FTLE ridges and Lagrangian saddle locations were identified for a series of 12 time-resolved snapshots at each of the 129 planes across the channel height. Using an adaptive cross-correlation algorithm by Dantec DYNAMICSTUDIO for every two sequential snapshots of cyan saddles, one average

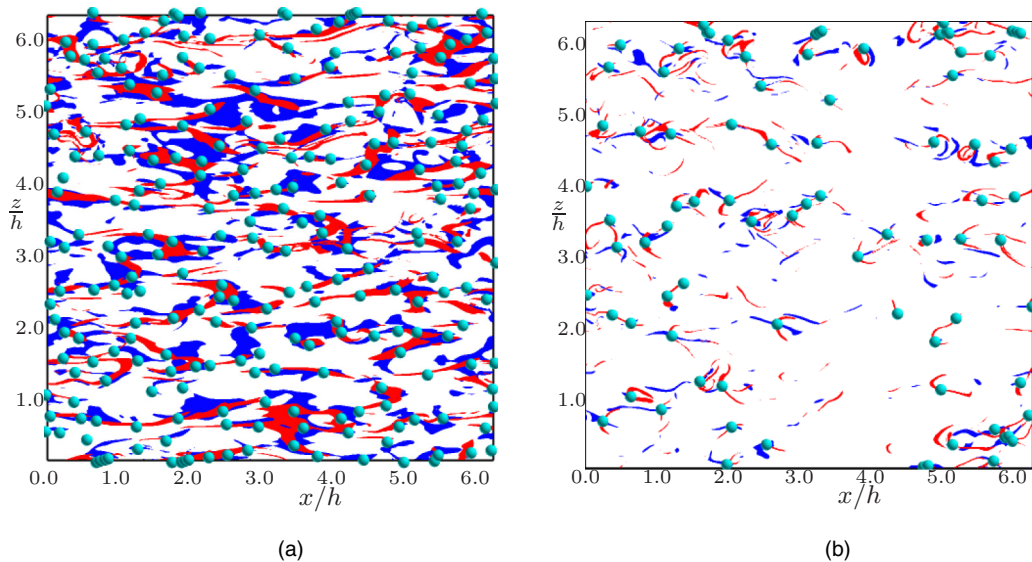


FIG. 3. Instantaneous snapshots of pFTLE ridges (blue) and nFTLE ridges (red) (values above $0.65\Lambda_{\max}$) at (a) $y^+ = 10.5$ and (b) $y^+ = 49.6$ in the turbulent channel simulation. Lagrangian saddles are highlighted by cyan circles.

streamwise velocity of the saddles at each plane was then calculated for each image pair. The algorithm is an iterative and adaptive cross-correlation-based displacement estimator combined with window shifting, window deformation, and subpixel analysis. In particle image velocimetry analysis, it iteratively adjusts the size and the shape of the individual interrogation areas during processing in order to adapt to local particle densities and flow gradients. For the current study, the streamwise convection velocity of saddles in each pair of snapshots was estimated from saddle displacements inside an interrogation area that was chosen to be the whole two-dimensional plane. This resulted in one average saddle velocity per instant in time per plane, which were then averaged together. The structure convection velocity was non-dimensionalized using the friction velocity: $u_c = u_{\text{conv}}/u_\tau$.

In Fig. 4, the averaged structure streamwise convection velocity is shown as a function of wall-normal distance. For comparison, the channel mean streamwise velocity $\bar{u} = u_{\text{mean}}/u_\tau$ is also included as a solid blue curve on the same axes. Error bars of one standard deviation of the resulting convection velocity are shown in red and are less than 10% of the mean velocity for most sections of the channel. The exceptions to this are planes close to the channel center, due to the existence of fewer saddles in this region, and planes very close to the wall, where the saddles are inconsistent due to the fact that the time scales of the flow are much shorter than the integration time. The plane-averaged transverse convection velocities of Lagrangian saddles for all the planes have near-zero mean values and have an average standard deviation of 3% of the mean convecting velocity, with a maximum of 11%.

The structure convection velocity u_c is approximately 10–15 % less than the mean profile velocity \bar{u} for a large segment of the channel width: $-0.92 < y/h < 0.92$ ($y^+ > 14$). Close to the wall ($y^+ \leq 14$), the velocity of the coherent structures is larger than the channel mean profile velocity. While this is consistent with the physical interpretation that coherent structures will travel faster than the viscous-dominated mean velocity close to the wall, the average velocity data in that region may not be statistically converged. Even though the channel mean velocity reaches zero close to the wall, the vortex structure convection velocity could be significant in the region due to perturbations caused by coherent structures advecting away from the wall. Kim *et al.* observed that the structure convection velocities are slightly smaller than the local mean velocity for portions of the channel away from the wall ($y^+ > 15$), but that they are higher near the wall ($y^+ < 15$), which agrees well

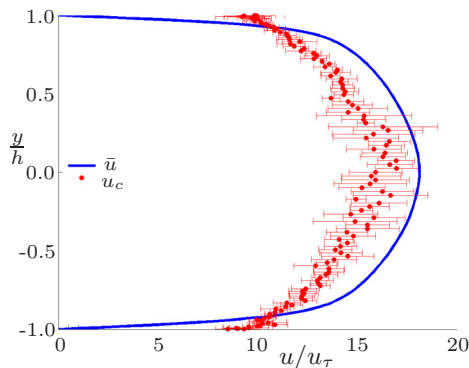


FIG. 4. Plane-averaged velocity of Lagrangian saddles in the turbulent channel simulation, plotted against wall-normal distance (red). These data are compared with the simulation mean streamwise velocity profile (blue). The error bars in the figure are one standard deviation of the measured Lagrangian saddle convection velocity in the plane.

with the current result [39,40]. The previous authors found that in sections near the wall ($y^+ < 15$) the structure convection velocity stays constant at 55% of the centerline velocity while the local mean velocity decreases until it is zero at the wall, indicating that the movement of coherent structures in this region is dominated by convection not viscosity.

The current study, which used automatic tracking of Lagrangian saddles, was consistent with previous results that used correlations of velocity and pressure. This shows the validity of using Lagrangian saddles to track coherent structures directly, avoiding the fluctuating velocity or pressure components that can be sensitive to small errors typically found in experimental data. FTLE ridges, and therefore Lagrangian saddle points found from them, are robust to small-magnitude or short-duration velocity field errors [10].

IV. VORTEX SHEDDING, SURFACE PRESSURE, AND FORCE IN BLUFF BODY SEPARATION

The FTLE can be instrumental not only in tracking individual structure motion, but also in detecting phenomenological events in their evolution, such as formation [41], shedding [25,31], and destruction [15]. To study vortex shedding, the wake behind a circular cylinder was considered, which is a canonical flow in the study of bluff bodies. At Reynolds numbers greater than 47, an unsteady wake develops behind the circular cylinder and results in periodic shedding of vortices in the classic von Kármán vortex street [42]. Gerrard [43] proposed that the vortices are shed due to the entrainment of fluid from the wake on the opposite side of the current vortex formation. The entrained fluid has opposite vorticity from the forming vortex, which causes the vortex to detach from the cylinder and move downstream. This vortex shedding causes oscillating fluid forces on the cylinder that can lead to failure due to structural fatigue [44,45].

To study the relationship among these fluctuating forces, the surface pressure distribution, and the coherent structure dynamics, one needs the temporally and spatially resolved static pressure information. Nishimura and Taniike [46] looked into the relationship between fluctuating lift and the stagnation and separation point locations on a circular cylinder and found that the von Kármán vortices forming downstream of the cylinder locally lowered the static pressure on the surface of the cylinder, even upstream of the separation point. The separation point is defined as the location where the wall shear stress is zero ($\tau_w = \mu du/dy|_{y=0} = 0$) and decreasing with respect to increasing angular location ($d\tau_w/d\theta < 0$), where $\theta = 0$ is taken to be the mean upstream stagnation point location. In this section we compare the spatial pressure distribution and its temporal evolution with the behavior and timing of Lagrangian shedding identification methods.

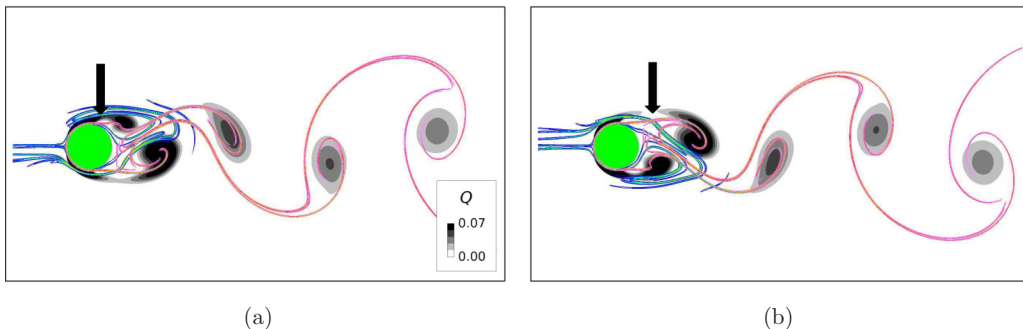


FIG. 5. Instantaneous snapshots of positive- and negative-time FTLE ridges (blue and red, respectively, with values above $0.67\Lambda_{\max}$) in the flow around a circular cylinder (represented by a green circle) with vortex cores visualized by Q (grey contours): (a) $t/T = 0.22$ and (b) $t/T = 0.82$. The Lagrangian saddle is highlighted by a black arrow.

Data from a two-dimensional simulation generated by Reger, advised by Taira and Cattafesta at Florida State University, which used the CHARLES solver developed by Cascade Technologies [47], was used for a full study of the cylinder near-wake and surface. CHARLES employs a second order finite volume method in space and a third order Runge-Kutta scheme in time. The coefficients of pressure, lift, and drag matched well with a similar simulation conducted by Inoue and Hatakeyama [48]. The code used an r, θ O-grid mesh with a constant $\Delta\theta = 0.725^\circ$ and an increasing Δr as the distance from the cylinder increased. The domain extended 200 diameters in the radial direction, and the velocity and pressure data generated on this grid were interpolated onto an x, y grid using bicubic interpolation. The data have a temporal resolution of 55 velocity files per period, and were run at $Ma = 0.2$ with $Re = 150$. The FTLE was calculated using an integration time of two shedding periods ($\tau = 2T$) and was selected to yield well-defined FTLE ridges. As long as the integration time is long enough to allow the tracked particles to sufficiently separate ($\tau \geq 0.5T$), changes in the integration time have a negligible effect on the location of the FTLE ridges in the flow field, consistent with Refs. [16,17].

Results

The near-wake region behind the circular cylinder is first visualized at two instants in time in Fig. 5, chosen to highlight the Lagrangian saddles. The FTLE ridges can be seen in blue (repelling ridge, pFTLE) and red (attracting ridge, nFTLE), and the vortex cores are located as regions where $Q > 0.01 Q_{\max}$ with grey contours. The color bar for Q is kept identical for all figures. Flow is from left to right, and the cylinder is shown in green. The development of the von Kármán vortex street can be seen as the dark grey regions of Q that are shed in an alternating pattern from the top and bottom halves of the cylinder. The Lagrangian saddle of interest, found at the intersection of the nFTLE and pFTLE ridges, is indicated by the black arrow. This saddle is located upstream of the clockwise-rotating vortex forming and shedding from the upper surface of the cylinder. A second saddle can be observed on the bottom half of the cylinder surface in the latter half of the shedding period, corresponding to the formation of the oppositely signed vortex.

Figure 6 displays a zoomed-in view of the cylinder wake. The attracting nFTLE ridges (red) wrap around the outside boundaries of the vortices as they form, separate, and convect downstream. The repelling pFTLE ridges (blue) form the boundaries between vortices as well as between forming vortices and the cylinder surface. The vortex center, found as the location of maximum Q within the vortex of interest, is highlighted by a red O and the Lagrangian saddle associated with that vortex is highlighted by a red X.

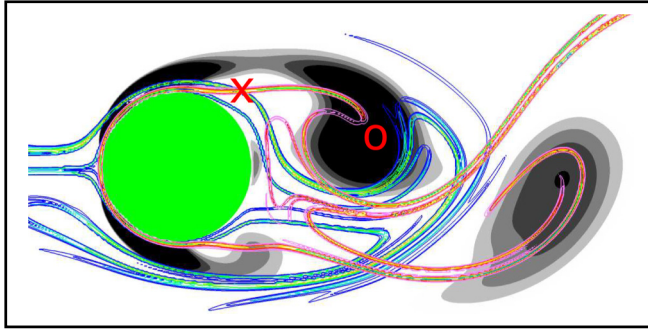


FIG. 6. pFTLE (blue), nFTLE (red), and Q criterion (grey contours) behind a circular cylinder (green) at $t/T = 0.55$. The Lagrangian saddle is highlighted by a red X and the vortex center is highlighted by a red O.

Rockwood *et al.* [1] tracked this Lagrangian saddle by hand and showed that, as the vortex forms, its corresponding Lagrangian saddle remains nearly stationary and attached to the cylinder surface. This saddle originates as a half saddle at the time-varying separation location which fluctuates around the mean separation location of 115° . As the vortex sheds, the saddle lifts off and accelerates away from the cylinder surface as shown in Fig. 7. The non-dimensional distance on the y axis is the distance from the Lagrangian saddle to a fixed point that is located at the closest point on the cylinder's surface to the initial saddle location. A solid black line is fit to the near-zero motion of the saddle (red diamonds) at early times in the vortex shedding period, while the vortex is still attached and forming. As the forming vortex continuously grows in size, the location of the vortex center (blue squares) also moves downstream, but with a higher slope that is slowly increasing. Near $t/T = 0.44$, the saddle accelerates away from the cylinder surface, which is observed as the departure of the red diamonds from the solid black line. In contrast, there is no distinct change in the speed of the vortex center found by the maximum Q value. Around $t/T = 0.90$, the vortex center has reached a constant velocity, shown by a dashed black line, as it convects downstream. At the same time, the saddle finishes accelerating to its final velocity, which matches that of the vortex center, and is also shown by a dashed black line (both dashed black lines have the same

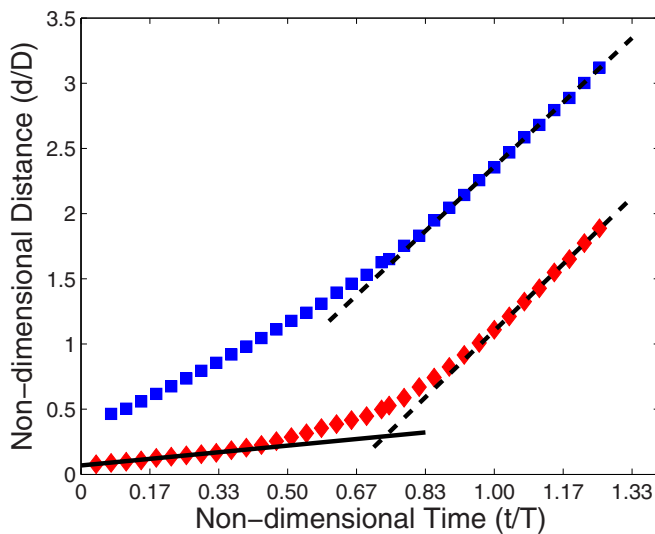


FIG. 7. Distance from cylinder to vortex center (blue squares) and Lagrangian saddle (red diamonds).

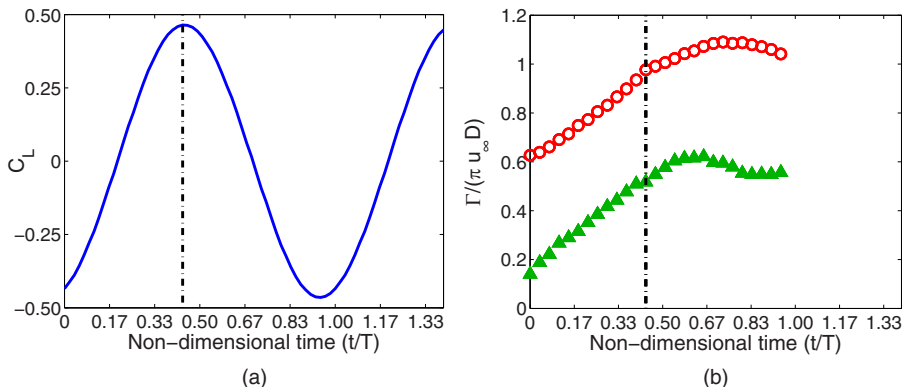


FIG. 8. (a) Coefficient of lift per unit span, $C_L(t)$, for the cylinder and (b) the normalized circulation for a vortex forming and shedding from the cylinder at $Re = 150$ at the time of Lagrangian saddle lift-off (black dash-dotted line).

slope). While the trace of the saddle location shows a dramatic change in slope, the trace of the vortex center has only a subtle, continuous change in slope. Since this change in slope is small and based on instantaneous velocity field gradients, it would be sensitive to errors in the velocity field in experimental or three-dimensional data.

The beginning of the acceleration of the Lagrangian saddle away from the cylinder is the criterion used to define the vortex shedding time, which occurs at $t/T = 0.44$. This acceleration of the Lagrangian saddle is indicative of the vortex beginning to travel downstream from the near-wake region it occupied during the vortex formation process. As this saddle sheds, so does a pFTLE ridge that had lain on the cylinder surface. The space between the shed pFTLE ridge and the cylinder surface then sees new entrainment of fluid into the region in which the next clockwise vortex will form. Another option to choose the vortex shedding time may be to choose the intersection of the solid and dashed lines in Fig. 7 at $t/T = 0.75$. However, this time does not connect to any topological changes, or a change in the behavior of the vortex or saddle. At that time, the vortex and the Lagrangian saddle are in the process of accelerating to the far field vortex convection speed as they shed from the cylinder. For these reasons, the saddle acceleration at $t/T = 0.44$ was used to indicate the beginning of the vortex shedding process.

1. Fluctuating cylinder lift and vortex circulation

The timing of the Lagrangian saddle acceleration provides a clear indication of when the vortex begins to shed from a wake dynamics perspective, but further physical insight can be gained by comparing the shedding time with the fluctuating lift experienced by the cylinder and the circulation of the shedding vortex. The lift coefficient per unit span on the cylinder [$C_L = L/(0.5\rho_\infty U_\infty^2 D)$] was found by integrating the static pressure distribution on the cylinder surface and calculating the force component per unit span in the vertical direction, L . Results from this calculation are displayed in Fig. 8(a), where it is observed that the maximum coefficient of lift is approximately 0.5, which agrees with previously published work [48]. As will be shown in Fig. 11, the pressure decreases on the top half of the cylinder in the first half of the shedding period, which results in the increase in lift during that portion of the period. The vortex shedding time inferred from the Lagrangian saddle lift off ($t/T = 0.44$) is shown in Fig. 8(a) by the vertical dash-dotted line. This time indicates the initial shedding of the vortex, and here is shown to correspond to the maximum lift. After this time the vortex begins convecting downstream, so it has a decreased effect on the cylinder pressure distribution.

Vortex separation and shedding can be described as a process in which the shear layer stops feeding circulation to the forming vortex, and the vortex does not pinch off until it reaches its maximum

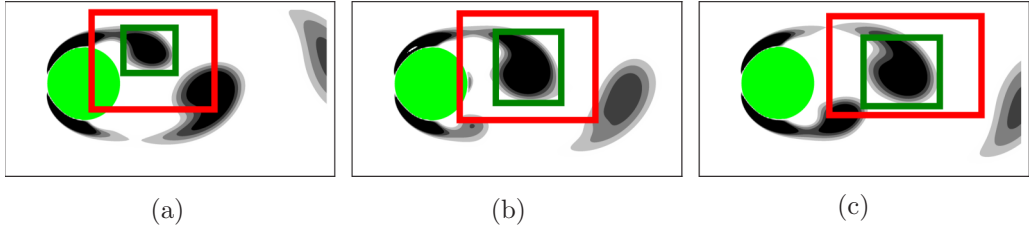


FIG. 9. Circulation area during (a) vortex formation ($t/T = 0.29$) and (b, c) shedding ($t/T = 0.58$ and $t/T = 0.78$, respectively).

circulation [34]. The circulation of the vortex forming and shedding from the upper cylinder surface was calculated using two different areas and is shown in Fig. 8(b) for comparison with the lift history and Lagrangian shedding time. The green bounding box for the circulation was determined by locating the distance from the vortex center to the contour of $0.01 Q_{\max}$ in the downstream and transverse directions, and using that as the distance to the respective rectangular box boundary in each direction. This bounding box enclosed the boundaries of the vortex and cut out the majority of the shear layer when the vortex is near the cylinder, as shown by the green box in Fig. 9(a). This was done intentionally to avoid the variable effect of the shear layer as the vortex and corresponding circulation area travel downstream. The circulation values [green triangles in Fig. 8(b)] are smaller than those found by Green and Gerrard [49], demonstrating the dependence of the circulation calculation on the size and shape of the bounding box. When the box is made large enough to include the majority of the shear layer, the value for maximum circulation is above 1.0 and is comparable to the value found by Green and Gerrard [49]. This is shown with the red box in Fig. 9, and the resulting time history of circulation in this area is shown as the open red circular symbols in Fig. 8(b).

Figure 8(b) shows that the times of maximum circulation for the two circulation areas used ($t/T = 0.65$ and $t/T = 0.73$) are later than the shedding time found by the Lagrangian saddle departure ($t/T = 0.44$). It is interesting to note that, by including more of the shear layer, the time of peak circulation is even later after the peak in lift. The disparity between the lift and circulation peak times may be due to the fact that while the shear-containing fluid that will constitute a portion of the shed vortex has shed from the cylinder surface, it has not yet been fed into the vortex core as defined by the bounding box even after it begins moving away from the cylinder surface. It is difficult to determine the exact time at which the shear layer stops feeding the vortex using a quantity such as the Q criterion, as the contours are often determined by a user-selected threshold ($Q = 0.01 Q_{\max}$ in this work). An integrated calculation of circulation shows it more clearly, but, while this information is useful for understanding the flow physics, it is still not a good method for determining the shedding time of the vortex because of its reliance on user-defined boundaries and its propensity to include portions of nearby shear layers. Tracking the Lagrangian saddle acceleration is not subject to the same user decisions about calculation area or thresholds and is here shown to correspond with the extrema in vertical force.

2. Pressure distribution at time of vortex shedding

While the acceleration of the Lagrangian saddle has been inferred to indicate the time of vortex shedding, the FTLE calculation used to find the Lagrangian saddle track relies on future data, which are not available on the fly. For this reason, the static pressure distribution on the cylinder surface was investigated to determine if the time evolution of the surface pressure correlates well with the lift off of the saddle. Figure 10 displays the time history of fluctuating pressure, $C'_p(t)$, at four angular locations along the cylinder surface, where 0° is taken as the mean location of the upstream stagnation point. $C'_p(t)$ is defined as $C'_p(t) = (p - \bar{p} - p_\infty)/(0.5\rho U_\infty^2)$, where p is the pressure, \bar{p} is the time average of pressure at that location, p_∞ is the free stream pressure, ρ is the fluid density, and U_∞ is the free stream velocity. $C'_p(t)$ is compared to the track of the Lagrangian saddle as in Fig. 7.

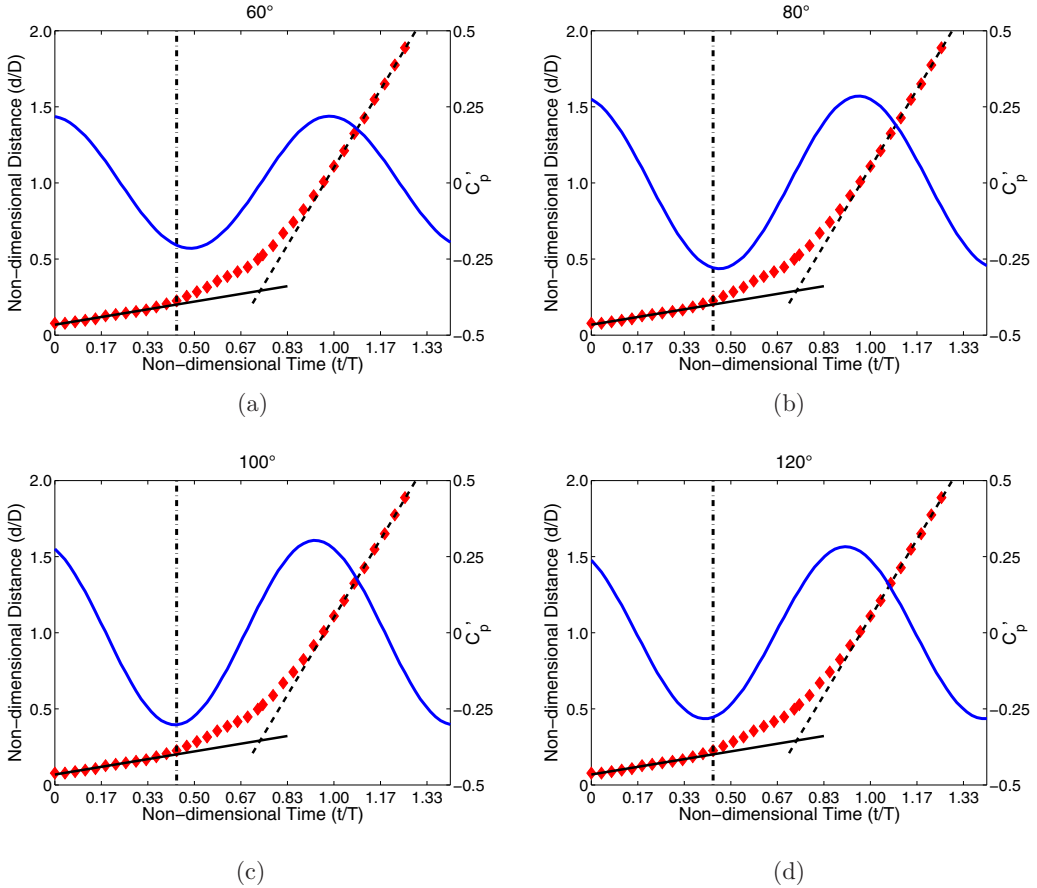


FIG. 10. $C_p'(t)$ (blue curves) at (a) 60° , (b) 80° , (c) 100° , and (d) 120° with saddle locations, and Lagrangian saddle distance to cylinder (red diamonds).

The vertical dash-dotted line indicates the time ($t/T = 0.44$) at which the Lagrangian saddle, and therefore the vortex, begins to shed from the cylinder surface.

As a vortex forms in the upper shear layer of the cylinder, it induces low pressure on the top half of the cylinder. As the vortex gains in strength, the pressure across the top half continues to decrease. When the vortex sheds, the pressure begins to increase again on that side of the cylinder. Because of this, it is expected that there is a minimum in pressure that occurs on the upper surface of the cylinder when the vortex is about to shed. Depending on the distance from the vortex core, the time at which the minimum in pressure occurs will vary. At a location 60° from the upstream stagnation point, as shown in Fig. 10(a), the pressure does not start to increase until after the saddle has accelerated away from the cylinder. It is inferred that this location is too far upstream from the vortex for the local pressure to be well correlated with the vortex shedding from the cylinder surface. As locations further downstream along the cylinder surface are considered, the pressure at 80° [Fig. 10(b)] still has not reached a minimum before the vortex sheds, but at the 100° location the pressure reaches its minimum just as the Lagrangian saddle is beginning to accelerate away from the cylinder surface [Fig. 10(c)]. Downstream of this region, at 120° [Fig. 10(d)], the pressure increases before the Lagrangian saddle acceleration away from the cylinder surface. The 100° location is also notable because it is just upstream of the mean separation location of 115° . This region just upstream of the separation point has previously been shown to contain a strong fluctuating pressure signal from the formation and

shedding of von Kármán vortices [50]. The current results show that this region is also closely tied to the von Kármán vortex shedding time identified by the Lagrangian saddle acceleration.

3. Time history of pressure at saddle departure location

Because the minimum pressure at a location 100° from the upstream stagnation point was found to correspond with the shedding time of the Lagrangian saddle, the pressure at this location is compared with vortex center motion, saddle motion, and total surface pressure distribution in Fig. 11. In the right-hand column, all four rows compare the Lagrangian saddle tracks with $C_p'(t)$ at 100° as in Fig. 7. The vertical dash-dotted line in these panels corresponds to the time used to plot the distribution of the fluctuating pressure coefficient and the wake visualizations in the center and left-hand columns, respectively, in the same row. In the left-hand column, the FTLE (blue and red ridges) and Q criterion (grey contours) are used to visualize the near wake of the cylinder (green circle). In these figures, flow is from left to right, and the Lagrangian saddle (red X) and vortex center (red O) locations in the wake are indicated. In the center column the C_p distribution around the circular cylinder at the given time is displayed, along with the relative locations of the saddle (red X), vortex center (red O), and measurement location for the time-resolved pressure shown in the right-hand column (the red line inside the cylinder points to the measurement location on the cylinder surface in the center column). The cylinder is outlined in black, and the radial labels apply to the magnitude of C_p (blue) across the cylinder surface at each angular location.

The pressure has a spatial maximum at the upstream stagnation point at a mean location of 0° . There is a favorable pressure gradient (pressure decreases as angular distance along the cylinder surface increases) on both the upper and lower surfaces of the cylinder near the upstream stagnation point. In this region, the fluid is accelerating around the cylinder, and stays attached. Once the minimum pressure is reached in the range of $\pm(70^\circ-80^\circ)$, an adverse pressure gradient begins, associated with a decrease in tangential velocity. This adverse pressure gradient ultimately leads to flow reversal and separation. The mean separation angle is at 115° , but the separation point fluctuates with the shedding phase, which is consistent with results from the literature [51].

As the vortex begins forming in Fig. 11(a) the pressure is relatively high along the upper half of the cylinder [Fig. 11(b)], and the Lagrangian saddle stays near the surface of the cylinder. In Fig. 11(d) the vortex has grown larger, as is observed by the increase in size of the grey (Q) region just behind the cylinder, but is still considered to be attached since the Lagrangian saddle remains on the cylinder surface. As the vortex grows in size and strength, the pressure on the upper half of the cylinder decreases, as shown by the blue C_p curve moving closer to the cylinder surface in Fig. 11(e). This trend continues until $t/T = 0.44$ [Figs. 11(g)–11(i)], when the vortex begins to lift away from the cylinder along with the Lagrangian saddle, at the same time as the pressure at 100° reaches its minimum. At $t/T = 0.58$ [Figs. 11(j)–11(l)], the pressure has begun to increase along the upper half of the cylinder as the vortex convects downstream. After this time the Lagrangian saddle continues to accelerate downstream until it reaches the convection speed of the vortex around $t/T = 0.9$, as shown in Fig. 7.

Current results have been computed for the flow around a circular cylinder at $Re = 150$. The mean separation location varies significantly with changing Reynolds number, so a similar variation in the static pressure location for correlation is expected. Sensor placement for detecting Lagrangian dynamics in a range of regimes or applications may need to be configured or calibrated for different Reynolds numbers or applications, but it should be possible to determine an appropriate sensor arrangement and to quantify its efficacy in determining the shedding behavior in a range of periodic flows.

V. DISCUSSION

An investigation into numerical simulations of the flow around a circular cylinder and in a fully developed turbulent channel found that the trajectory and phenomenological evolution of coherent structures could be determined by tracking Lagrangian saddles located at the intersections of positive- and negative-time FTLE ridges. Automatic tracking of the Lagrangian saddles in a turbulent channel

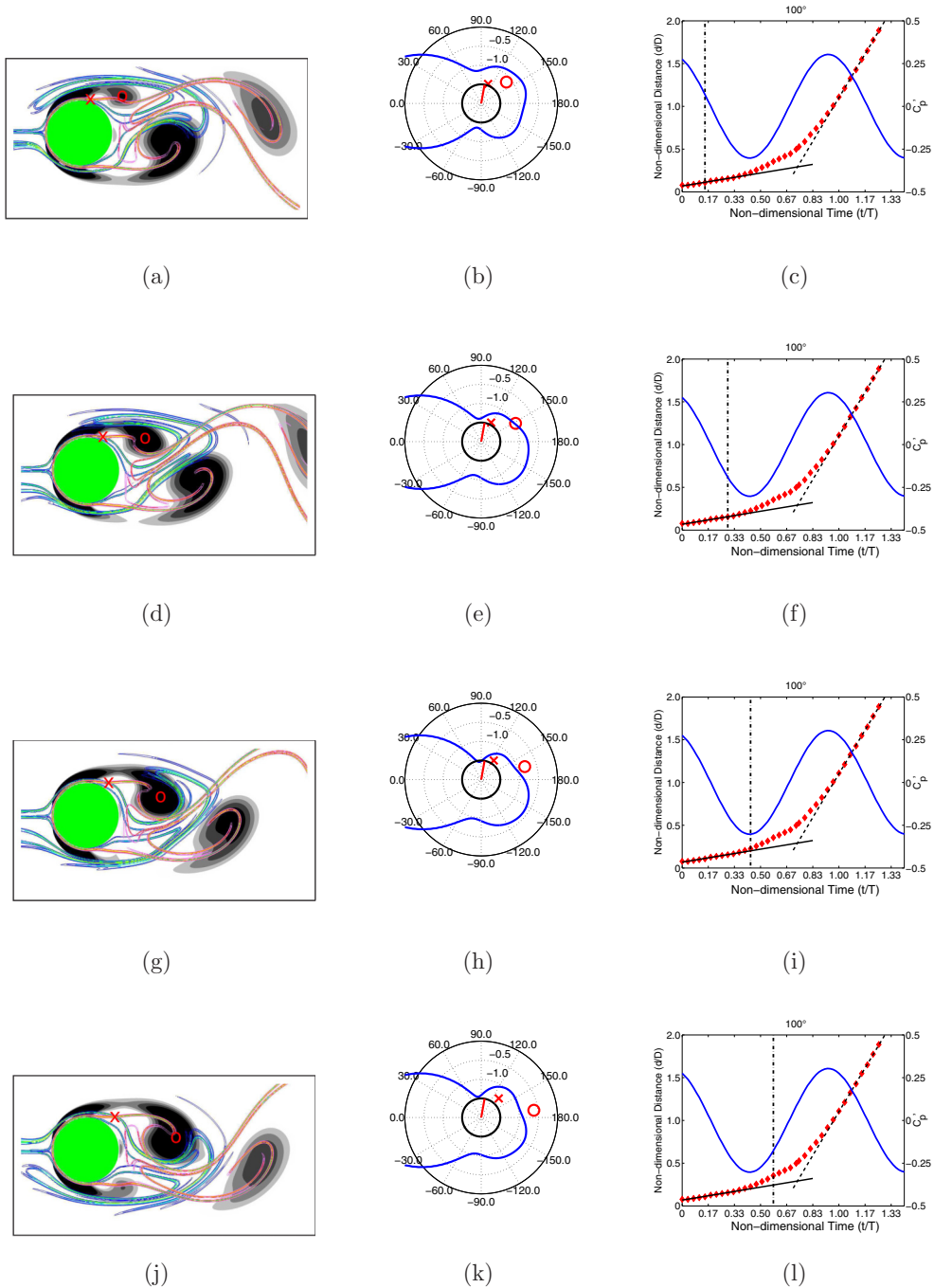


FIG. 11. pFTLE (blue), nFTLE (red), and Q criterion (grey contours) behind a circular cylinder (green) in left-hand column. C_p (blue), saddle location (red X in left-hand and center columns and red diamond in right column), and vortex center location (red O) at different times. FTLE and Q in cylinder wake at (a) $t/T = 0.15$, (d) $t/T = 0.29$, (g) $t/T = 0.44$, and (j) $t/T = 0.58$; C_p distribution around cylinder at (b) $t/T = 0.15$, (e) $t/T = 0.29$, (h) $t/T = 0.44$, and (k) $t/T = 0.58$; and (c, f, i, l) $C_p'(t)$ at 100° with saddle locations.

demonstrated that coherent structures that are outside of the viscous-dominated region moved at a convection speed that mimics the mean streamwise velocity profile, but with a magnitude 10–15 % lower. Structures in the near-wall region convect at a speed higher than the mean streamwise velocity, possibly due to coherent structure advection away from the wall. Both these findings are consistent with previously published results and demonstrate the potential of using this method to develop an automatic tracking algorithm that will provide statistical quantities of coherent structure dynamics in complex, three-dimensional flows. In particular, this study confirmed the ability of an automatic tracking algorithm using Lagrangian saddles to capture similar physics of turbulent coherent structure streamwise motion to that already established in the literature. The FTLE analysis, however, can also provide a more complete three-dimensional physical representation than the previously employed velocity and pressure correlation methods.

In massively-separated flows, in particular for vortex shedding off of a circular cylinder, tracking the Lagrangian saddles determined that a Lagrangian saddle accelerates away from the cylinder surface at the shedding time of the associated vortex. This shedding time was compared with the shedding time determined by the force history, the spatial track of the vortex center, the vortex circulation, and the time-resolved distribution of the pressure coefficient on the cylinder surface. The force history agreed well with the Lagrangian saddle shedding time, but the motion of the vortex center and the vortex circulation yielded shedding times that did not correspond to a minimum in pressure or a maximum in force on the cylinder.

While the Lagrangian saddle dynamics provided useful information about vortex trajectories and dynamics, they cannot directly be determined in real time. To address this, the time-resolved static pressure distribution on a circular cylinder was also used to examine the relationship between the pressure on the cylinder surface and the motion of the Lagrangian saddles. The surface static pressure 15° upstream of the mean separation point was found to reach its minimum just as the vortex was shed from the cylinder, indicated by the Lagrangian saddle beginning to accelerate away from the cylinder surface. This relationship makes possible the detection of vortex shedding, described objectively by the Lagrangian saddle motion, simply using common sensors at or around that angular location. The information acquired from a few specifically placed pressure sensors could then be used to inform closed-loop flow control around bluff bodies, to deploy high-lift devices to prevent stall, or to inform fuel injection levels in a mixing application. In the case of turbulent wall-bounded flows, the tracked motion of coherent structures could also be correlated with signatures of pressure or shear stress at the wall for further model development or to inform drag-reducing flow control strategies.

In both applications, using the Lagrangian saddles to track the coherent structures yielded an objective point in space tied to their location, which enabled the implementation of automatic tracking algorithms after the computation of the requisite FTLE fields. Automatic tracking of coherent structures, regardless of the complexity of the flow they are in, the Reynolds number, or the turbulence intensity, allows for the robust application of quantitative analysis techniques and criteria to determine the behavior of structures in a variety of flows.

ACKNOWLEDGMENTS

The authors would like to thank their collaborators at Florida State University for kindly providing the numerical cylinder data. This work was supported by the Air Force Office of Scientific Research under Award No. FA9550-14-1-0210.

-
- [1] Matthew P. Rockwood, Kunihiko Taira, and Melissa A. Green, Detecting vortex formation and shedding in cylinder wakes using Lagrangian coherent structures, *AIAA J.* **55**, 15 (2017).
 - [2] Philippe Miron and Jérôme Vétel, Towards the detection of moving separation in unsteady flows, *J. Fluid Mech.* **779**, 819 (2015).

- [3] Philippe Miron, Jérôme Vétel, and André Garon, On the flow separation in the wake of a fixed and a rotating cylinder, *Chaos* **25**, 087402 (2015).
- [4] Laurent Graftieux, Marc Michard, and Nathalie Grosjean, Combining PIV, POD and vortex identification algorithms for the study of unsteady turbulent swirling flows, *Meas. Sci. Technol.* **12**, 1422 (2001).
- [5] Julian C. R. Hunt, A. A. Wray, and Parviz Moin, Eddies, streams, and convergence zones in turbulent flows, in *Studying Turbulence Using Numerical Simulation Databases 2* (Stanford University, Stanford, CA, 1988), Vol. 1, pp. 193–208.
- [6] R. Perrin, M. Braza, E. Cid, S. Cazin, F. Moradei, A. Barthet, A. Sevrain, and Y. Hoarau, Near-wake turbulence properties in the high Reynolds number incompressible flow around a circular cylinder measured by two- and three-component PIV, *Flow Turbul. Combust.* **77**, 185 (2006).
- [7] M. Braza, R. Perrin, and Y. Hoarau, Turbulence properties in the cylinder wake at high Reynolds numbers, *J. Fluids Struct.* **22**, 757 (2006).
- [8] K. Onoue and K. S. Breuer, Vortex formation and shedding from a cyber-physical pitching plate, *J. Fluid Mech.* **793**, 229 (2016).
- [9] George Haller, Distinguished material surfaces and coherent structures in 3D fluid flows, *Phys. D (Amsterdam, Neth.)* **149**, 248 (2001).
- [10] George Haller, Lagrangian coherent structures from approximate velocity data, *Phys. Fluids* **14**, 1851 (2002).
- [11] Michael R. Allshouse and Jean-Luc Thiffeault, Detecting coherent structures using braids, *Phys. D (Amsterdam, Neth.)* **241**, 95 (2012).
- [12] George Haller and Francisco J. Beron-Vera, Geodesic theory of transport barriers in two-dimensional flows, *Phys. D (Amsterdam, Neth.)* **241**, 1680 (2012).
- [13] G. Haller and F. J. Beron-Vera, Coherent Lagrangian vortices: The black holes of turbulence, *J. Fluid Mech.* **731**, R4 (2013).
- [14] Daniel Blazevski and George Haller, Hyperbolic and elliptic transport barriers in three-dimensional unsteady flows, *Phys. D (Amsterdam, Neth.)* **273**, 46 (2014).
- [15] Melissa A. Green, Clarence W. Rowley, and Alexander J. Smits, The unsteady three-dimensional wake produced by a trapezoidal pitching panel, *J. Fluid Mech.* **685**, 117 (2011).
- [16] J. A. Bourgeois, P. Sattari, and R. J. Martinuzzi, Coherent vortical and straining structures in the finite wall-mounted square cylinder wake, *Int. J. Heat Fluid Flow* **35**, 130 (2012).
- [17] L. Kourentis and E. Konstantinidis, Uncovering large-scale coherent structures in natural and forced turbulent wakes by combining PIV, POD, and FTLE, *Exp. Fluids* **52**, 749 (2011).
- [18] Pengfei Lei, Jiazhong Zhang, Kailun Li, and Ding Wei, Study on the transports in transient flow over impulsively started circular cylinder using Lagrangian coherent structures, *Commun. Nonlinear Sci. Numer. Simul.* **22**, 953 (2015).
- [19] Ali Bahadır Olcay, Investigation of a wake formation for flow over a cylinder using Lagrangian coherent structures, *Prog. Comput. Fluid Dyn.* **16**, 126 (2016).
- [20] F. J. Beron-Vera, M. J. Olascoaga, and G. J. Goni, Oceanic mesoscale eddies as revealed by Lagrangian coherent structures, *Geophys. Res. Lett.* **35**, L12603 (2008).
- [21] S. C. Shadden, M. Astorino, and J. Gerbeau, Computational analysis of an aortic valve jet with Lagrangian coherent structures, *Chaos* **20**, 017512 (2010).
- [22] M. Weldon, T. Peacock, G. B. Jacobs, M. Helu, and G. Haller, Experimental and numerical investigation of the kinematic theory of unsteady separation, *J. Fluid Mech.* **611**, 1 (2008).
- [23] J. D. Eldredge and K. Chong, Fluid transport and coherent structures of translating and flapping wings, *Chaos* **20**, 017509 (2010).
- [24] Clara O’Farrell and John O. Dabiri, Pinch-off of non-axisymmetric vortex rings, *J. Fluid Mech.* **740**, 61 (2014).
- [25] Karen Mulleners and Markus Raffel, The onset of dynamic stall revisited, *Exp. Fluids* **52**, 779 (2012).
- [26] Philip du Toit and Jerrold Marsden, Horseshoes in hurricanes, *J. Fixed Point Theory Appl.* **7**, 351 (2010).
- [27] Michael R. Allshouse and Thomas Peacock, Lagrangian based methods for coherent structure detection, *Chaos* **25**, 097617 (2015).

- [28] George Haller, A variational theory of hyperbolic Lagrangian coherent structures, *Phys. D (Amsterdam, Neth.)* **240**, 574 (2011).
- [29] Yong Wang, George Haller, Andrzej Banaszuk, and Gilead Tadmor, Closed-loop Lagrangian separation control in a bluff body shear flow model, *Phys. Fluids* **15**, 2251 (2003).
- [30] Clara O'Farrell and John O. Dabiri, A Lagrangian approach to identifying vortex pinch-off, *Chaos* **20**, 017513 (2010).
- [31] Yangzi Huang and Melissa A. Green, Detection and tracking of vortex phenomena using Lagrangian coherent structures, *Exp. Fluids* **56**, 1 (2015).
- [32] M. S. Chong, A. E. Perry, and B. J. Cantwell, A general classification of three-dimensional flow fields, *Phys. Fluids A* **2**, 765 (1990).
- [33] Jinhee Jeong and Fazle Hussain, On the identification of a vortex, *J. Fluid Mech.* **285**, 69 (1995).
- [34] Matthew J. Ringuette, Michele Milano, and Morteza Gharib, Role of the tip vortex in the force generation of low-aspect-ratio normal flat plates, *J. Fluid Mech.* **581**, 453 (2007).
- [35] Doug Lipinski and Kamran Mohseni, A ridge tracking algorithm and error estimate for efficient computation of Lagrangian coherent structures, *Chaos* **20**, 017504 (2010).
- [36] Ali B. Olcay, Tait S. Pottebaum, and Paul S. Krueger, Sensitivity of Lagrangian coherent structure identification to flow field resolution and random errors, *Chaos* **20**, 017506 (2010).
- [37] S. J. Kline, W. C. Reynolds, F. A. Schraub, and P. W. Runstadler, The structure of turbulent boundary layers, *J. Fluid Mech.* **30**, 741 (1967).
- [38] Stephen K. Robinson, Coherent motions in the turbulent boundary layer, *Annu. Rev. Fluid Mech.* **23**, 601 (1991).
- [39] John Kim, Parviz Moin, and Robert Moser, Turbulence statistics in fully developed channel flow at low Reynolds number, *J. Fluid Mech.* **177**, 133 (1987).
- [40] John Kim and Fazle Hussain, Propagation velocity of perturbations in turbulent channel flow, *Phys. Fluids A* **5**, 695 (1993).
- [41] Melissa A. Green, Clarence W. Rowley, and George Haller, Detection of Lagrangian coherent structures in three-dimensional turbulence, *J. Fluid Mech.* **572**, 111 (2007).
- [42] C. H. K. Williamson, Vortex dynamics in the cylinder wake, *Annu. Rev. Fluid Mech.* **28**, 477 (1996).
- [43] J. H. Gerrard, The mechanics of the formation region of vortices behind bluff bodies, *J. Fluid Mech.* **25**, 401 (1966).
- [44] G. S. Baarholm, C. M. Larsen, and H. Lie, On fatigue damage accumulation from in-line and cross-flow vortex-induced vibrations on risers, *J. Fluids Struct.* **22**, 109 (2006).
- [45] M. A. Tognarelli, S. Taggart, and M. Campbell, Actual VIV fatigue response of full scale drilling risers: With and without suppression devices, in *Proceedings of the ASME 27th International Conference on Offshore Mechanics and Arctic Engineering* (American Society of Mechanical Engineers, New York, 2008).
- [46] H. Nishimura and Y. Taniike, Aerodynamic characteristics of fluctuating forces on a circular cylinder, *J. Wind Eng. Ind. Aerodyn.* **89**, 713 (2001).
- [47] Yaser Khalighi, Frank Ham, Joseph W. Nichols, S. Lele, and Parviz Moin, Unstructured large eddy simulation for prediction of noise issued from turbulent jets in various configurations, in *Proceedings of the 17th AIAA/CEAS Aeroacoustics Conference (32nd AIAA Aeroacoustics Conference)* (AIAA, Reston, VA, 2011).
- [48] O. Inoue and N. Hatakeyama, Sound generation by a two-dimensional circular cylinder in a uniform flow, *J. Fluid Mech.* **471**, 285 (2002).
- [49] R. B. Green and J. H. Gerrard, Vorticity measurements in the near wake of a circular cylinder at low Reynolds numbers, *J. Fluid Mech.* **246**, 675 (1993).
- [50] R. Perrin, M. Braza, E. Cid, S. Cazin, A. Barthet, A. Sevrain, C. Mockett, and F. Thiele, Obtaining phase averaged turbulence properties in the near wake of a circular cylinder at high Reynolds number using POD, *Exp. Fluids* **43**, 341 (2007).
- [51] Ming-Hsun Wu, Chih-Yung Wen, Ruey-Hor Yen, Ming-Cheng Weng, and An-Bang Wang, Experimental and numerical study of the separation angle for flow around a circular cylinder at low Reynolds number, *J. Fluid Mech.* **515**, 233 (2004).